

Testing the inverse-Compton catastrophe scenario in the intra-day variable blazar S5 0716+71

II. A search for intra-day variability at millimetre wavelengths with the IRAM 30 m telescope^{*}

I. Agudo¹, T. P. Krichbaum¹, H. Ungerechts², A. Kraus¹, A. Witzel¹, E. Angelakis¹, L. Fuhrmann^{1,3,4}, U. Bach^{1,4},
S. Britzen¹, J. A. Zensus¹, S. J. Wagner⁵, L. Ostorero^{5,6}, E. Ferrero⁵, J. Gracia⁷, and M. Grewing⁸

¹ Max-Planck-Institut für Radioastronomie, Auf dem Hügel 69, 53121 Bonn, Germany
e-mail: iagudo@mpi-fr-bonn.mpg.de

² Instituto de Radio Astronomía Milimétrica, Avenida Divina Pastora 7, Local 20, 18012 Granada, Spain

³ Dipartimento di Fisica, Università di Perugia, via A. Pascoli, 06123 Perugia, Italy

⁴ INAF, Osservatorio Astronomico di Torino, via Osservatorio 20, 10025 Pino Torinese (TO), Italy

⁵ Landessternwarte Heidelberg-Königstuhl, Königstuhl, 69117 Heidelberg, Germany

⁶ Tuorla Observatory, University of Turku, Väisäläntie 20, 21500 Piikkiö, Finland

⁷ Department of Physics, University of Athens, Panepistimiopolis, 157 84 Zografos, Athens, Greece

⁸ Institut de Radio Astronomie Millimétrique, 300 rue de la Piscine, Domaine Universitaire de Grenoble,
38406 Saint Martin d'Hères, France

Received 5 December 2005 / Accepted 31 May 2006

ABSTRACT

We report on a densely time sampled polarimetric flux density monitoring of the BL Lac object S5 0716+71 at 86 GHz and 229 GHz. The source was observed with the IRAM 30 m telescope at Pico Veleta within a coordinated multi-frequency observing campaign, which was centred around a 500 ks INTEGRAL observation during November 10 to 16, 2003. The aim of this campaign was to search for signatures of inverse-Compton catastrophes through the observation of the broad-band variability of the source. At 86 GHz, S5 0716+71 showed no intra-day variability, but showed remarkable inter-day variability with a flux density increase of 34% during the first four observing days, which cannot be explained by source extrinsic causes. At this frequency, making use of a new calibration strategy, we reach a relative rms accuracy of the flux density measurements of 1.2%. Although the flux density variability at 229 GHz was consistent with that at 86 GHz, the larger measurement errors at 229 GHz do not allow us to detect, with high confidence, inter-day variations at this frequency. At 86 GHz, the linear polarization fraction of S5 0716+71 was unusually large ($15.0 \pm 1.8\%$). Inter-day variability in linear polarization at 86 GHz, with significance level $\geq 95\%$; $\sigma_P/\langle P \rangle = 15\%$ and $\sigma_\chi = 6^\circ$, was observed during the first four observing days. From the total flux density variations at the synchrotron turnover frequency (~ 86 GHz) we compute an apparent brightness temperature $T_B^{\text{app}} > 1.4 \times 10^{14}$ K at a redshift of 0.3, which exceeds by two orders of magnitude the inverse-Compton limit. A relativistic correction for T_B^{app} with a Doppler factor $\delta > 7.8$ brings the observed brightness temperature down to the inverse Compton limit. A more accurate lower limit of $\delta > 14.0$, consistent with previous estimates from VLBI observations, is obtained from the comparison of the 86 GHz synchrotron flux density and the upper limits for the synchrotron self-Compton flux density obtained from the INTEGRAL observations. The relativistic beaming of the emission by this high Doppler factor explains the non-detection of “catastrophic” inverse-Compton avalanches by INTEGRAL.

Key words. galaxies: active – galaxies: BL Lacertae objects: general – galaxies: BL Lacertae objects: individual: S5 0716+71 – radio continuum: galaxies – radiation mechanisms: non-thermal – polarization

1. Introduction

The effect of intra-day variability (IDV) of radio loud active galactic nuclei (AGN) in the radio bands was discovered in 1986 (Witzel et al. 1986; Heeschen et al. 1987) and since then led to controversial discussions about its physical origin. Most of the objects presenting radio IDV appear compact – when are observed in the radio and optical bands –, their relativistic jets are highly core-dominated on VLBI scales and exhibit high brightness temperatures (e.g. Wagner & Witzel 1995).

IDV is a common phenomenon in extragalactic flat spectrum radio sources and is observed, at centimetre wavelengths, in about 10% to 25% of all objects of this class (Quirrenbach et al. 1992; Kedziora-Chudczer et al. 2001; Lovell et al. 2003). The “classical IDV” (of type II, as defined in Heeschen et al. 1987) is characterised by variability amplitudes $\lesssim 20\%$ and variability time-scales between 0.5 days and 2 days. In parallel to the variability of the total flux density, similar or even faster variations of the linear polarization (Quirrenbach et al. 1989; Kraus et al. 1999a,b, 2003) and of the circular polarization (Macquart et al. 2000) are observed. Intensity and polarization variations

^{*} Appendices A and B are only available in electronic form at <http://www.edpsciences.org>

can be correlated or anti-correlated (e.g. Wagner et al. 1996; Macquart et al. 2000; Qian et al. 2002).

Observations of IDV sources in the radio and millimetre bands are particularly important, since they reveal the highest apparent brightness temperatures ($T_B \propto \nu^{-2}$; e.g. Readhead 1994). However, the observed radio emission might also be severely affected by interstellar scintillation (ISS), which is unavoidable because of the small intrinsic sizes of IDV sources (Rickett 1990). It is known that, for high Galactic latitude blazars, the amplitude of IDV due to the effect of interstellar scintillation rapidly decreases with frequency for $\nu \gtrsim 5$ GHz (e.g. Rickett 1990; Rickett et al. 1995; Beckert et al. 2002). In such case and for a source whose size is constant with frequency, the ISS-induced variability amplitude scales as $\propto \nu^{-2}$ (e.g. Beckert et al. 2002). Hence, any rapid and large amplitude source variability seen at millimetre (or shorter) wavelengths should not be strongly affected by ISS. Therefore, monitoring of IDV sources at mm-bands is particularly important to determine whether the observed IDV is mainly source extrinsic (scintillation), due to source intrinsic processes, or a mixture of both.

S5 0716+71 (hereafter 0716+714) is an extremely active BL Lac object which varies on time scales from less than one hour to months, from radio to X-rays (e.g. Wagner et al. 1996; Kraus et al. 2003; Raiteri et al. 2003). Although the optical spectrum of 0716+714 appears featureless, even with 4 m class telescopes, the absence of any signature of a host galaxy (in deep images) sets a lower limit to its redshift of $z > 0.3$ (Wagner et al. 1996). Therefore, only lower limits to the brightness temperature of the source can be derived. The strongest constraint on the brightness temperature of this source comes from the observed short variability time-scales at radio wavelengths, which sets, via the causality argument, an upper limit to the source size of a few tens of micro-arcseconds. During the last decade the source has been observed repeatedly in simultaneous centimetre wavelength campaigns (Wagner et al. 1990, 1996; Otterbein et al. 1999; Kraus et al. 2003; Raiteri et al. 2003), during which it typically showed IDV. 0716+714 is the only IDV source which has shown simultaneous variability-time-scale transitions in the radio and optical bands, which have been interpreted as evidence for source intrinsic variability (Quirrenbach et al. 1991; Wagner & Witzel 1995; Qian et al. 1996). The correlation between the radio spectral index and the optical flux suggested that the radiation was produced by the same particle population (Qian et al. 1996). Additional arguments for the relevance of the intrinsic origin of the IDV in 0716+714 come from the variability amplitude, which increases from radio to optical, and the recently detected IDV at a wavelength of 9 mm (Kraus et al. 2003). Both effects contradict expectation for the frequency dependence of ISS.

If IDV is produced by the intrinsic properties of AGN, very small angular sizes of the emitting regions (of a few micro-arcseconds) are inferred from their short variability time-scales. This usually implies apparent brightness temperatures several orders of magnitude larger than the inverse-Compton (IC) limit ($\lesssim 10^{12}$ K, Kellermann & Pauliny-Toth 1969; Readhead 1994; Kellermann 2003). For incoherent synchrotron sources of radiation, this limit could be violated only during short time ranges, because the high energy photon densities at the IC-limit should lead to the rapid cooling of the emitting region through the IC scattering of the synchrotron radiation. This process is known as the *inverse-Compton catastrophe*. The relativistic beaming of the radiation coming from the emitting region (Rees 1966) has been proposed as a likely cause to explain the systematic violation of the IC-limit (e.g. Wagner & Witzel 1995). Other

scenarios, as coherent synchrotron radiation, which is an unconventional but not impossible process in AGN, have been proposed (e.g. Benford 1992). However, the inverse-Compton catastrophe scenario cannot still be ruled out (Wagner & Witzel 1995).

A coordinated broad-band observing campaign – centred around a 500 ks INTEGRAL¹ observation during November 10 to 16, 2003 – was performed to search for signatures of inverse-Compton catastrophes on a flaring state of 0716+714 through the correlation of the broad-band variability of the source. The ground-based observations were performed with the VLBA, the Effelsberg 100 m, the Metsähovi 13.7 m, the IRAM 30 m, the JCMT, the HHT, and the Kitt Peak 12 m telescopes and the optical-IR telescopes of the WEBT² collaboration. The first analysis of the broad-band (from radio to soft γ -rays) observations (Ostorero et al. 2006) do not show obvious correlation between the intra-day optical variability and the inter-day radio variability displayed by the source. Although the apparent brightness temperatures of 0716+714 largely exceeded the IC-limit at radio wavelengths, no evidence of IC avalanches was seen in the INTEGRAL data.

In this paper we report on the results and implications of the first polarimetric millimetre wavelength IDV observations of 0716+714, which were performed (within the above-mentioned campaign) with the IRAM 30 m radio telescope during the period November 10 to 18, 2003. A combined discussion of the radio, millimetre and sub-millimetre single dish data set will be presented by Fuhrmann et al. (in prep.). Forthcoming papers will describe more detailed analysis of the optical observations and more sophisticated theoretical modelling of the broad-band data set.

2. Observations and data reduction

2.1. Observations

The observations presented here were specially planned to achieve accurate measurements of the total flux density with a typical temporal resolution better than 1 h. To achieve this goal, we observed 0716+714 and a number of suitable calibrators continuously for ~ 18 h on each day during November 10 to 18, 2003, using the IRAM 30 m telescope at Pico Veleta (Granada, Spain). The observations were interrupted by intervals where the elevation of the program source was lower than 20° or when the weather conditions were inappropriate for 86 GHz observations. Under these conditions, accurate antenna and gain calibrations were not possible.

The receiver-cabin optic system of the IRAM 30 m telescope is optimised to observe with up to four different receivers at the same time (Wild 1999). We made use of the A100, A230, B100 and B230 heterodyne receivers of the telescope, which simultaneously observed at both 86 GHz (A100 and B100, at $\lambda \approx 3.5$ mm, where λ is the wavelength) and 229 GHz (A230 and B230, at $\lambda \approx 1.3$ mm). This standard observing set-up uses a grid to divide the incoming signal into two orthogonal linear polarizations and then two Martin-Pupplet interferometers (one per polarization) to split the 86 GHz and the 229 GHz frequency bands. Hence, at each observing band, the A- and B-receivers were sensitive to two orthogonal linear polarizations. This allowed us to obtain linear polarization information at 86 GHz. Receiver A230 was not stable enough to provide reliable measurements and hence we lost the polarization information at

¹ INTErnational Gamma-Ray Astrophysics Laboratory.

² Whole Earth Blazar Telescope.

229 GHz. The observing bandwidths at 86 GHz and 229 GHz were 0.5 GHz and 1 GHz, and the typical single side band system temperatures were ~ 100 K and ~ 400 K, respectively.

All the measurements were performed in “beam-switching” mode, using a chopper wheel to subtract the emission contribution from the sky. During the continuous chopping (at a frequency of ≈ 7 Hz) the telescope beam was moved to a $70''$ off-position. The individual measurements were performed by repeated cross-scans over the source position in azimuth and elevation. The number of sub-scans in each measurement and for each source was chosen according to the flux density of the source, with more sub-scans on the fainter objects. For technical reasons, the number of sub-scans were multiples of four and ranged between 4 and 16. 0716+714 was observed with a “duty cycle” of about 1 to 2 measurements every 60 min. Also six bright and point-like extragalactic radio sources (S5 0212+735, S5 0633+734, S5 0836+710, S4 1642+690, S5 1803+784, S5 1928+738, which will be called hereafter by their catalogue codes) were observed with a duty cycle of at least one measurement every hour. Their known variability characteristics at cm-wavelengths and location on the sky allowed us to assume that they were non-variable on time-scales of days and so they were suitable as secondary calibrators³. For the determination of the absolute flux density scale, we observed two planets (Mars and Uranus) at least once per day and we also included two bright and compact HII regions (W3 OH, K3-50A) and the planetary nebula NGC 7027 in the measurement cycle every 4 h to 5 h.

The frequent observation of the target source and the primary and secondary calibrators, in combination with our non-standard data reduction procedure, enabled us to calibrate the measurements with unprecedented precision. This was possible thanks to the accurate determination of the dependence of calibration on elevation and time from the measurements of the calibrators. This method has been successfully proven on previous observations of IDV (e.g. Quirrenbach et al. 1992; Kraus et al. 2003), which achieved relative calibration accuracies better than 1 % at radio frequencies. The method also allows for the empirical determination of the internal calibration errors without the need of a detailed knowledge of the individual sources of error affecting the measurements.

2.2. Total flux density data reduction

The initial step of the data calibration used a method equivalent to the “chopper-wheel⁴” calibration (e.g. Kutner & Ulich 1981) to translate the detected power (measured in arbitrary units) into calibrated and opacity corrected antenna temperatures (T_A^* in K). The “chopper-wheel” procedure uses measurements of a hot and a cold load, both at known temperatures, and the sky temperature to compute the calibration factor for each measurement. At the IRAM 30 m telescope, this calibration factor takes into account the total absorption and thermal emission of the atmosphere, which are computed by an atmospheric radiative transfer model (see Kramer 1997 and references therein for details). For our adopted observing set-up at the IRAM 30 m telescope, this is

³ In Sect. 3.1 we show that this assumption was true for all the observed extragalactic calibrators but 1642+690.

⁴ Note that the “chopper-wheel” calibration procedure (which at the 30 m telescope does not use a chopper wheel) is totally unrelated to the “beam-switching” mode (which uses the chopper wheel). This paradoxical nomenclature has been maintained for historical reasons.

Table 1. rms of the normalised measurements of the secondary calibrators (but 1642+690) after each of the data reduction stages.

Frequency	Data reduction stage							
	1	2	3	4	5	6	7	8
86 GHz	12	11	5	4	4	1.4	1.2	1.2
229 GHz	120	100	30	19	...	16	16	16

the standard initial calibration, which is performed in “real time” by the software of the telescope.

The post-observation data reduction was performed following an incremental strategy in different stages, further improving the calibration accuracy after each of them. After each correction the data were inspected and edited following different criteria, depending on the previous correction. The rms of the normalised measurements of the secondary calibrators are listed in Table 1 to show how much each of the corrections improved the calibration. Here we explain the corrections applied on each of the data reduction stages:

Stage 1: we first averaged for each scan independently the sub-scans in azimuth and in elevation. Then, we fitted a Gaussian profile to the average of each of the two scanning directions. The amplitude of the Gaussian corresponds to T_A^* in both directions.

Stage 2: using the measured FWHM of the telescope beam ($\approx 28''$ at 86 GHz and $\approx 11''$ at 229 GHz), we were able to correct the amplitudes measured on the two directions for the observed (small, typically $\lesssim 3''$) telescope pointing errors. These corrections were typically smaller than 5% at 86 GHz and 25% at 229 GHz. After this correction, we averaged the measurements from the azimuth and elevation directions to produce a single T_A^* measurement per receiver and scan.

Stage 3: subsequently, we corrected for elevation dependent effects on the data, i.e. caused by gravitational deformation of the telescope dish. For this purpose, we used the antenna gain curves given by Greve et al. (1998). After this correction ($\lesssim 2\%$ at 86 GHz and $\lesssim 5\%$ at 229 GHz), the data did not show any significant elevation dependence.

Stage 4: after that, we removed the most obvious systematic time-dependent variations, i.e. gain decreases (which were $\lesssim 10\%$ at 86 GHz and $\lesssim 30\%$ at 229 GHz) mainly produced by abrupt ambient temperature changes. The corresponding gain corrections were computed by making use of the densely time-sampled measurements of all our secondary calibrators besides 1642+690, and assuming that they were constant during our observations. The latter was confirmed by our variability analysis (see Sect. 3.1).

Stage 5: at 86 GHz, it was also possible to correct for a small relative gain difference of receivers A100 and B100 ($\approx 1.035\%$), detected by comparing good quality measurements of unpolarized calibrators. After that, the averaging of the results from A100 and B100 enabled to reduce the uncertainties on the determination of the T_A^* measurements at 86 GHz. An accurate relative calibration of the A100 and B100 gains is also required to measure the linear polarization properties of the polarized sources at 86 GHz (see Appendix A and Sect. 2.3). Due to the lack of reliable measurements from the A230 receiver, these data improvements could not be performed for the 229 GHz data.

Stage 6: to further improve our calibration, an additional time-dependent correction, similar to the one explained on stage 4, was applied to correct for residual systematic time

Table 2. Absolute surface brightnesses (in Jy/beam) of Mars, Uranus, W3 OH, K3-50A and NGC 7027 adopted for the computation of the Kelvin-to-Jansky conversion factors of the 30 m telescope at 86 GHz and 229 GHz.

Source	UT days of Nov. 2003					
	11	12	13	14	15	16
86 GHz						
Mars ^a	149.75	146.88	144.08	141.33	138.65	136.02
Uranus ^a	7.06	7.05	7.04	7.03	7.01	7.01
W3 OH ^b				3.94		
K3-50A ^b				6.29		
NGC 7027 ^b				4.71		
229 GHz						
Mars ^a	691.16	683.33	675.51	666.71	659.92	652.17
Uranus ^a	32.88	32.83	32.77	32.72	32.67	32.61
W3 OH ^b				6.48		
K3-50A ^b				6.98		
NGC 7027 ^b				3.68		

^a Computed from the expressions given in Kramer (1997), and references therein, which take into account the angular size of the planets. The values given for Uranus were computed from an empirical model which used Mars as primary calibrator (Griffin & Orton 1993).

^b Obtained from averages of measurements performed during several years – before 1996 – at the IRAM 30 m telescope. These measurements were themselves calibrated through observations of planets. The sizes of these calibrators at 1.2 mm are given in Lisenfeld et al. (2000).

variations of the overall gain. The corrected gain variations were $\lesssim 5\%$ at 86 GHz and $\lesssim 20\%$ at 229 GHz on this stage.

Stage 7: then we derived the Kelvin-to-Jansky conversion factors (C_{KJ}) by comparing the measurements of Mars, Uranus, W3 OH, K3-50A and NGC 7027 (which are all of them unpolarized) with their assumed absolute surface brightnesses (Table 2). The final values, $C_{KJ}(86 \text{ GHz}) = (6.37 \pm 0.04) \text{ Jy/K}$ and $C_{KJ}(229 \text{ GHz}) = (9.3 \pm 0.3) \text{ Jy/K}$ are the result of the average of the different Kelvin-to-Jansky conversion factors computed from each of the above calibrators. The errors in C_{KJ} take into account the uncertainties of our measurements of the primary calibrators, but not the possible inaccuracies on the assumed values of their surface brightnesses. $C_{KJ}(86 \text{ GHz})$ and $C_{KJ}(229 \text{ GHz})$ were finally applied to all the data to obtain absolute flux density measurements (S in Jy) for 0716+714 and the secondary calibrators.

Note that the absolute surface brightnesses of Uranus, W3 OH, K3-50A and NGC 7027 were calibrated relative to those of Mars (Table 2, Griffin & Orton 1993; Kramer 1997). Hence, an additional 5% absolute calibration error, coming from uncertainties in the true martian temperatures (Griffin & Orton 1993), would have to be quadratically added to our absolute flux density results. However, as this does not affect our main relative variability analyses – based on measurements scaled to the same Kelvin-to-Jansky factor – the extra 5% error has not been added, unless explicitly indicated for each particular absolute flux density measurement.

Stage 8: finally, we performed an empirical estimate of the internal calibration errors, including those that could not be taken into account previously (mainly those affecting the gain corrections of data reduction steps 4, 5 and 6). This a posteriori error estimate was performed by computing the rms of the normalized flux density measurements of the assumed non-variable secondary calibrators (all of them except 1642+690), which resulted $\text{rms}_{86} = 1.2\%$ and $\text{rms}_{229} = 16\%$ for the 86 GHz and 229 GHz data, respectively. These quantities were finally added in quadrature to the error of each individual measurement on stage 7, which were initially computed from the $1-\sigma$ uncertainty estimates of the amplitude of the Gaussian profiles and were then propagated through the different averages and corrections of the data reduction procedure. The final relative errors of each

individual measurement were typically of $\sim 2\%$ at 86 GHz and $\sim 18\%$ at 229 GHz for 0716+714. As indicated above, an additional 5% factor should still be added quadratically to account for the absolute flux density errors.

Note that the small receiver-temperature changes monitored during the observations did not allow flux density fluctuations larger than $\sim 0.5\%$ either at 86 GHz or at 229 GHz. Hence, the residual rms_{86} and rms_{229} statistical uncertainties are most likely resulting from the small and rapid atmospheric fluctuations between independent measurements, which due to the limited time sampling could not be corrected.

It is worth to stress that the small $\text{rms}_{86} = 1.2\%$ characterises the excellent performance of the IRAM 30 m telescope and the stability of 86 GHz observations at the telescope site. This also demonstrates the ability for future high accuracy IDV studies at millimetre wavelengths.

2.3. Linear polarization data reduction

To extract the linear polarization information at 86 GHz we modelled the response of the two orthogonally polarized linear feeds of the receivers A100 and B100 to a partially linearly polarized source⁵. In Appendix A we show that, for our observing set-up at the IRAM 30 m telescope, these responses fulfil the following equations:

$$\frac{S_{A100}(i) + S_{B100}(i)}{2} = S_0(i), \quad (1)$$

$$S_{A100}(i) - S_0(i) = \frac{1}{2}P(i) \cos 2\left(\alpha(i) + \frac{\pi}{2}\right) \quad (2)$$

and

$$S_{B100}(i) - S_0(i) = \frac{1}{2}P(i) \cos 2(\alpha(i)), \quad (3)$$

⁵ We assumed a negligible degree of circular polarization (p_c), which is null for the observed Galactic sources and typically $< 1\%$ at cm and mm wavelengths for extragalactic AGN (Clemens Thum private communication; Homan & Lister 2006 and references therein). In particular, at 86 GHz the measured p_c of 0716+714 is $< 0.4\%$ (Clemens Thum, private communication).

where $S_{A100}(i)$ and $S_{B100}(i)$ are, respectively, the flux densities recorded by the receivers A100 and B100 at the time of the i th measurement, $S_0(i)$ is the total flux density of the source, $P(i)$ is its linearly polarized flux density and $\alpha(i)$ is the angle between the horizontal axis of the telescope's polarization reference plane (coincident with the B100 polarization axis) and the direction of polarization of the source at time i . The angle $\alpha(i)$ is defined as

$$\alpha(i) = \frac{\pi}{2} - \chi(i) + \eta(i) - \epsilon(i), \quad (4)$$

where $\chi(i)$ is the astronomical electric vector position angle (polarization angle hereafter) of the source (defined in the equatorial coordinate system from north to east). $\eta(i)$ and $\epsilon(i)$ are, respectively, the parallactic and elevation angles at the time of the i th measurement (see Appendix A and Thum et al. 2000). We estimated the magnitudes of $P(i)$ and $\chi(i)$ by performing independent fits on the equations (2) and (3) to the data. It was necessary to assume that the source did not vary in polarization during the time interval of each fit, $5 \text{ h} \leq t \leq 12 \text{ h}$. To reduce the final uncertainty of the results, the two independent estimates of $P(i)$ and $\chi(i)$ (from the independent fits of (2) and (3)) were averaged together.

Thum et al. (2003) reported that, for polarimetric measurements with the A100 and B100 receivers of the IRAM 30 m telescope, the main contribution to the instrumental polarization is produced by differences in the relative calibration of both receivers. As explained in Sect. 2.2, special care was taken to remove these calibration differences *i*) by correcting for the independent small pointing offsets (typically $\lesssim 3''$) and *ii*) by correcting for the gain ratio affecting the A100 and B100 receivers. Hence, the main component of the instrumental polarization is initially removed from the data through our calibration procedure.

To test this and to quantify the amount of spurious polarization still remaining in the data, we performed fits of the normalized (to $S_0(i)$) versions of equations (2) and (3) to the data of the unpolarized calibrators (Mars, Uranus, W3 OH, K3-50A and NGC 7027) over the whole observing time range. The result, $\langle p \rangle = (0.2 \pm 0.9)\%$, provides a measurement of the maximum instrumental linear polarization affecting our polarization fits, $p_{\text{inst}}^{\text{max}} = 1.1\%$, which we consider negligible for the purposes of our data analysis. The fact that $p_{\text{inst}}^{\text{max}}$ is of similar magnitude than rms_{86} indicates that, as for the total flux density measurements, our polarization accuracy is most likely limited by the statistical uncertainties induced by the small and rapid atmospheric fluctuations.

Such uncertainties are computed from the linear polarization fits. In the case of 0716+714, for time periods $t \lesssim 12 \text{ h}$, they lie in the range 1.2% to 3.4% for p and between $\sim 0.06 \text{ Jy}$ and $\sim 0.12 \text{ Jy}$ for P (see Sect. 3.2). The additional error (a 5% of the total flux density) coming from the inaccuracy on the absolute flux density scaling, has been added in quadrature wherever it was necessary for the final P results; i.e. only for non-relative variability results. In such cases, we explicitly indicate that this additional error was added.

The accuracy of our polarization angle estimates is better tested on sources with large linear polarization fraction, which should show large modulation amplitudes in functions (2) and (3), and hence should allow for a more accurate measurement of χ . Among our observed sources, 0716+714 was the most suitable one for such test, since it showed the highest polarization degree (see Sect. 3) and was better time sampled. The two independent fits of functions (2) and (3) to the 0716+714 data, over ten different time ranges of $t \lesssim 12 \text{ h}$ (Sect. 3.2), showed an

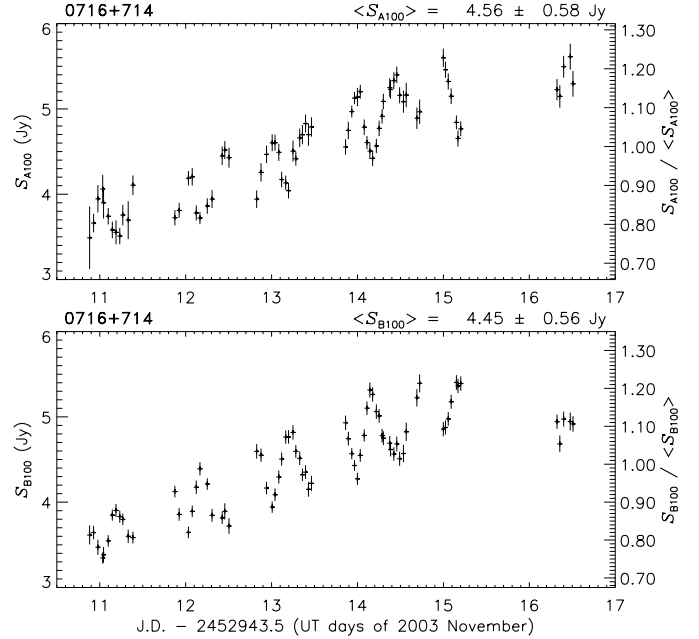


Fig. 1. Calibrated measurements of S_{A100} and S_{B100} for 0716+714 vs. time during 2003 November 10 to 16. The sinusoidal pattern is due to source polarization (see the text).

internal consistency of the χ estimates to a precision better than 0.5° . This demonstrates the accuracy of equations (2), (3) and (4) and the good orthogonality of the signals recorded by receivers A100 and B100. However, the statistical uncertainties on the determination of χ fail to be better than $\chi_{\text{inst}}^{\text{max}} = 1.1^\circ$ even for the polarization fits to the 0716+714 data over the whole observing time. Also for 0716+714, these uncertainties range between 1.8° and 9° for the ten time spans with $t \lesssim 12 \text{ h}$ (Sect. 3.2).

Note that the accuracy of *absolute* polarization angle measurements obtained from A100 and B100 data is driven by the accuracy of the orientation of their polarization axes (see Appendix A and Thum et al. 2000). Such orientations were calibrated with an accuracy of $\sim 1^\circ$ (Clemens Thum, private communication), which is therefore the better absolute polarization angle accuracy achievable with the A100 and B100 receivers. A corresponding error of 1° has been added quadratically to the χ statistical uncertainties of our measurements obtained for the whole observing time range, but not to those computed for shorter time spans – which are aimed at relative variability analyses –.

3. Results

In Fig. 1 we present plots of the resulting calibrated responses of receivers A100 and B100 to the 0716+714 emission during November 11 to 17. The curves show a remarkable increase of $\sim 1.5 \text{ Jy}$ in S_{A100} and S_{B100} during November 10 to 14 together with a large amplitude sinusoidal modulation, which has a characteristic periodicity of 12 h and has a phase difference of π rad between the S_{A100} and S_{B100} patterns. The main contribution to this modulation is explained by the right-hand terms of expressions (2) and (3), which are significant when the source is highly linearly polarized. Following (2) and (3), the linear polarization flux density of 0716+714 can be estimated from the amplitudes of the modulations of the S_{A100} and S_{B100} curves, which lie in the range $0.4 \text{ Jy} \leq P \leq 0.9 \text{ Jy}$. Hence, the curves in Fig. 1 represent the first evidence of a high degree of linear

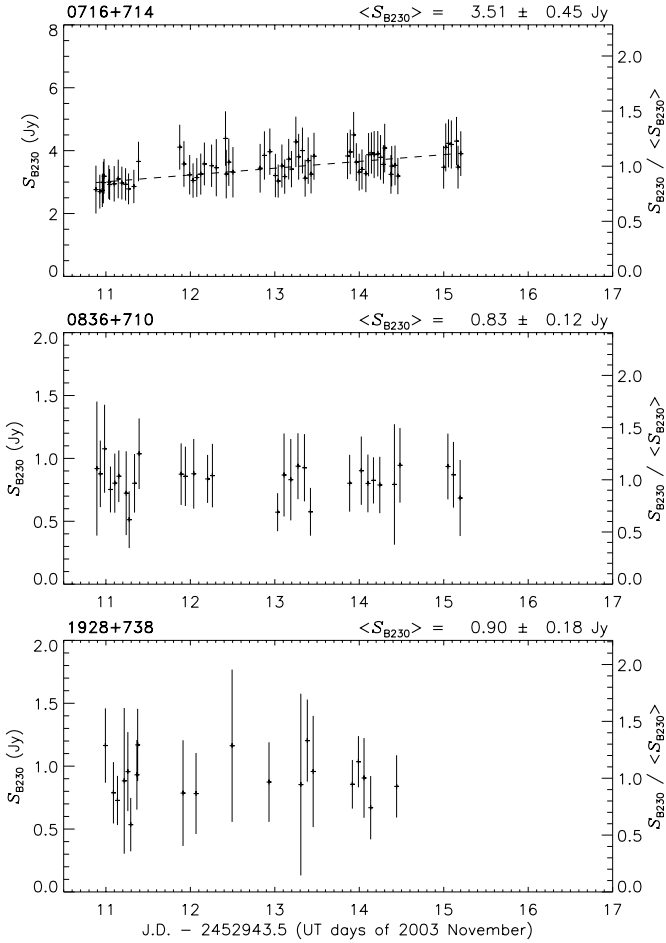


Fig. 2. Calibrated measurements of S_{B230} for 0716+714, 0836+710 and 1928+738 during 2003 November 10 to 15. The dashed line on the top inset represents the best linear fit to the 0716+714 light curve.

polarization ($10\% \lesssim p \lesssim 20\%$) in 0716+714 at 86 GHz. As far as we know, such a high linear polarization was never observed before in the integrated emission of 0716+714 in any radio to mm band.

In Fig. 2 we show the calibrated response of B230 to the 0716+714 emission during November 10 to 15. The larger measurement uncertainties at 229 GHz, which are typically $\sim 18\%$, do not allow us to detect IDV with amplitude lower than this level. Therefore, we are able to determine only the basic emission properties at this frequency. Since at 229 GHz 0716+714 does not show the expected 12 h periodic polarization modulation, then, within the errors, the response of B230 is a valid measurement of the source total flux density (S_{229}).

3.1. Total flux density

Accurate measurements of the 86 GHz flux densities ($S_{86}(i)$) were obtained by averaging together $S_{A100}(i)$ and $S_{B100}(i)$ (see Appendix A). The resulting evolution of $S_{86}(i)$ during the time range of our observations of 0716+714 is presented in Fig. 3 together with the light curves of the non-IDV sources 0836+710 and 1928+738. The latter demonstrate the accuracy of our calibration, which provided flux density measurements characterised by an $\text{rms}_{86} \approx 1.2\%$. This represents an unprecedented stability for 86 GHz measurements with the IRAM 30 m telescope.

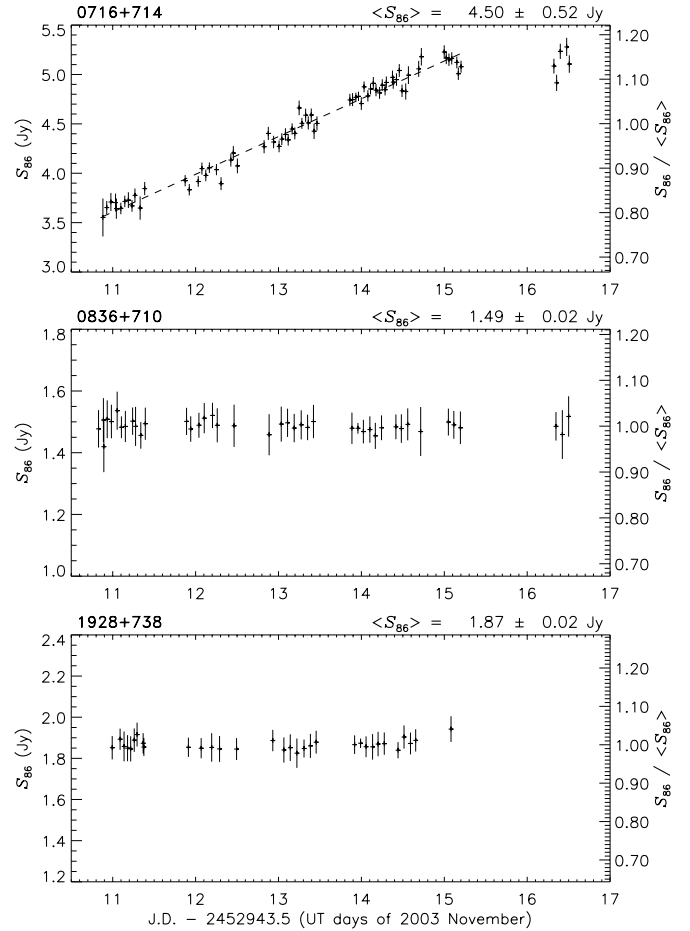


Fig. 3. Calibrated 86 GHz light curves of 0716+714, 0836+710 and 1928+738 during 2003 November 10 to 16. The dashed line on the top inset represents the best linear fit to the 0716+714 flux density evolution during 2003 November 10 to 15.

The variability of 0716+714 at 86 GHz appears to be dominated by a monotonous linear increase from $\langle S_{86} \rangle = (3.71 \pm 0.08)$ Jy during November 10 to 11 to $\langle S_{86} \rangle = (5.13 \pm 0.86)$ Jy during November 15 (with $\langle \rangle$ denoting averaging in time). During the ~ 5 h of data obtained on November 16, the source displayed a similar mean flux density of $\langle S_{86} \rangle = (5.12 \pm 0.13)$ Jy. The linear fit of the light curve from days 10 to 15 (Fig. 3) gives an increasing rate ($\dot{S}_{86}/\langle S_{86} \rangle$) of $(8.58 \pm 0.14)\%/ \text{day}$. The fit performed to the 229 GHz light curve gives $\dot{S}_{229}/\langle S_{229} \rangle = (6.2 \pm 1.7)\%/ \text{day}$, which shows a similar trend at both observing frequencies. This suggests that the variability at both 86 GHz and 229 GHz originates from the same region of the source and the same physical process.

To characterise the flux density variability of each source we used the statistical formulation described in Quirrenbach et al. (2000) and Kraus et al. (2003). In particular, we made use of the modulation index m , the variability amplitude Y , the reduced chi-squared χ_r^2 and the structure function $D(\tau)$. The corresponding definitions are summarised in Appendix B.

The computed statistical parameters for 0716+714 and the secondary calibrators are listed in Table 3 for both the 86 GHz and the 229 GHz data set. The computation of the variability amplitude Y was performed only for those sources that passed the chi-squared test (variable with significance level $>99.9\%$). As can be seen in the table, only 0716+714 showed such

Table 3. Statistical parameters characterising the variability of 0716+714 and the secondary calibrators during 2003 November 10 to 16.

Source	N	$\langle S \rangle$ [Jy]	σ_S [Jy]	m [%]	χ_r^2	Y [%]
$\nu = 86 \text{ GHz}, m_0 = 1.20 \%$						
0212+735	33	1.101	0.016	1.45	0.3	...
0633+734	25	0.942	0.018	1.90	0.4	...
0716+714	74	4.502	0.516	11.46	55.3	34.19
0836+710	42	1.486	0.020	1.36	0.1	...
1642+690*	24	1.044	0.060	5.73	1.6	...
1803+784	32	1.334	0.016	1.19	0.1	...
1928+738	32	1.866	0.024	1.31	0.1	...
$\nu = 229 \text{ GHz}, m_0 = 16.0 \%$						
0212+735	15	0.712	0.094	13.14	0.1	...
0633+734	15	0.621	0.085	13.72	0.1	...
0716+714	68	3.506	0.448	12.77	0.5	...
0836+710	31	0.830	0.123	14.77	0.3	...
1642+690*	8	0.744	0.254	34.17	0.5	...
1803+784	20	0.940	0.235	25.04	0.8	...
1928+738	20	0.904	0.177	19.54	0.4	...

* Although this source did not pass our chi-squared test, it displays much larger m and χ_r^2 than the remaining secondary calibrators, suggesting a higher variability.

Note: Y computation was only performed for 0716+714 at 86 GHz, the only case for which the variability chi-squared test was passed.

significant variability (at 86 GHz, but not at 229 GHz due to the larger uncertainties at that frequency).

Although 1642+690 formally did not pass this test, it displayed larger values of m and χ_r^2 than the remaining calibrators at both 86 GHz and 229 GHz (see Table 3), suggesting a weaker variability. In fact, its 86 GHz light curve (frequency at which the variability analysis is more accurate) is variable at confidence level $>95\%$. Based on this evidence, we excluded 1642+690 as secondary calibrator from the 86 GHz and 229 GHz data reduction.

The structure function $D(\tau)$ for 0716+714 at 86 GHz is shown in Fig. 4. The shape of this function provides the variability type classification of the observed sources (Heeschen et al. 1987; Kraus et al. 2003). The lack of pronounced maxima and of a saturation point in $D(\tau)$ on time lags shorter than two days allows us to classify 0716+714 as an IDV source of type I during the time range of our observations at 86 GHz. The local maximum appearing at a time lag of ~ 4 days characterises the time-scale of the monotonic increase of the flux density S_{86} . In agreement with this, and based on the same data set, Fuhrmann et al. (in prep.) report, from a more sophisticated estimate, a time-scale of $3.83^{+0.14}_{-0.15}$ days.

3.2. Polarization

The 86 GHz polarization estimates were obtained by fitting the functions (2) and (3), which relate directly the amplitudes and phases of such polarization patterns to the linearly polarized flux density P and electric vector position angle χ of the observed source, respectively. The fits performed for 0716+714 for $\lesssim 12$ h time bins (with a minimum of ten points per fit) are shown in Fig. 5. This time binning was chosen as the optimum to provide more than one P and χ measurement per day and the lowest possible uncertainties in their estimate. Polarization fits for $\lesssim 24$ h time bins and for the entire time range of the observations were

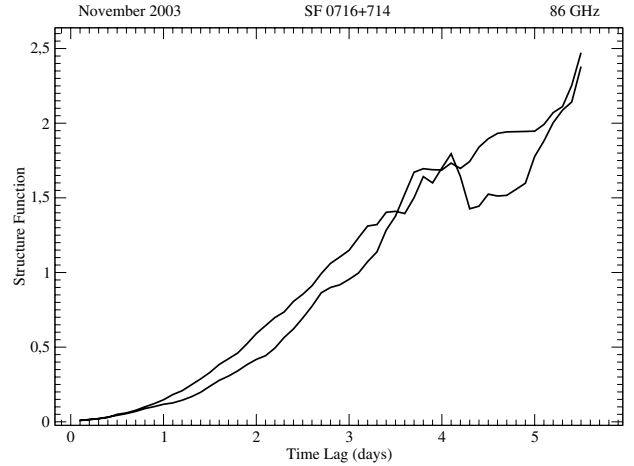


Fig. 4. $D(\tau)$ function for 0716+714 at 86 GHz. Since the data are unevenly sampled, we derived $D(\tau)$ using an interpolation procedure. A minimal interpolation interval of ~ 2.5 h (3 to 5 times larger than the typical S_{86} sampling time-range) was chosen. To assess the errors caused by the interpolation, $D(\tau)$ was derived twice, first by starting at the beginning of the time series and second by proceeding backwards.

also performed for both 0716+714 and the secondary calibrators (Fig. 6, Tables 4 and 5).

The fits presented in Fig. 5 confirm the previously mentioned high polarization level of 0716+714 at 86 GHz. The average polarization properties of the source (during our observations) were $\langle p \rangle = (15.0 \pm 1.8)\%$, or $\langle P \rangle = (0.68 \pm 0.23)$ Jy, and $\langle \chi \rangle = 31.4^\circ \pm 1.5^\circ$ (Table 4), where the errors of $\langle P \rangle$ and $\langle \chi \rangle$ take into account those from the absolute total flux density and polarization angle uncertainties, respectively (see Sect. 2). Such a high polarization degree is rather unusual for AGN at centimetre wavelengths, for which $p > 10\%$ is rarely observed even during flaring states (e.g. Aller et al. 1999) and typically $1\% \lesssim p \lesssim 6\%$. Synchrotron self-absorption, usually dominating at low centimetre radio frequencies, can reduce p (e.g. Pacholczyk 1970). However, low values of polarization degree are observed at centimetre wavelengths even for optically thin sources. Numerical simulations show that, in order to explain these low levels of polarization in compact radio sources, a large fraction of the magnetic field (typically 50%–70%) should be disordered in direction (e.g. Gómez, Alberdi & Marcaide 1993). The 15% polarization degree detected in 0716+714 might indicate a high level of magnetic field alignment in the region from which the 86 GHz emission originated.

In addition, one of the six observed AGN calibrators, 0212+735, also displays a polarization degree $p > 10\%$ and 0633+734 and 1803+784 show $p \approx 8\%$. These values are still high when compared with the typically observed polarization degrees at centimetre wavelengths. The fact that, at 86 GHz, more than 50% of the observed AGN display larger polarization degrees than those typically measured at centimetre wavelengths might suggest that the polarization degree in AGN increases with frequency. This would indicate higher ordering of the magnetic fields in the deeper regions of their jets observed in the millimetre bands respect to centimetre wavelengths. However, it is clear that our sampled set of AGN is not statistically significant enough to strongly support this hypothesis. The millimetre polarization survey performed by Thum et al. (in prep.) over more than 70 AGN during the summer of 2006 will certainly improve the statistics.

Inspection of Fig. 5 indicates time-dependent changes in both the amplitude and the phase of the fitted functions,

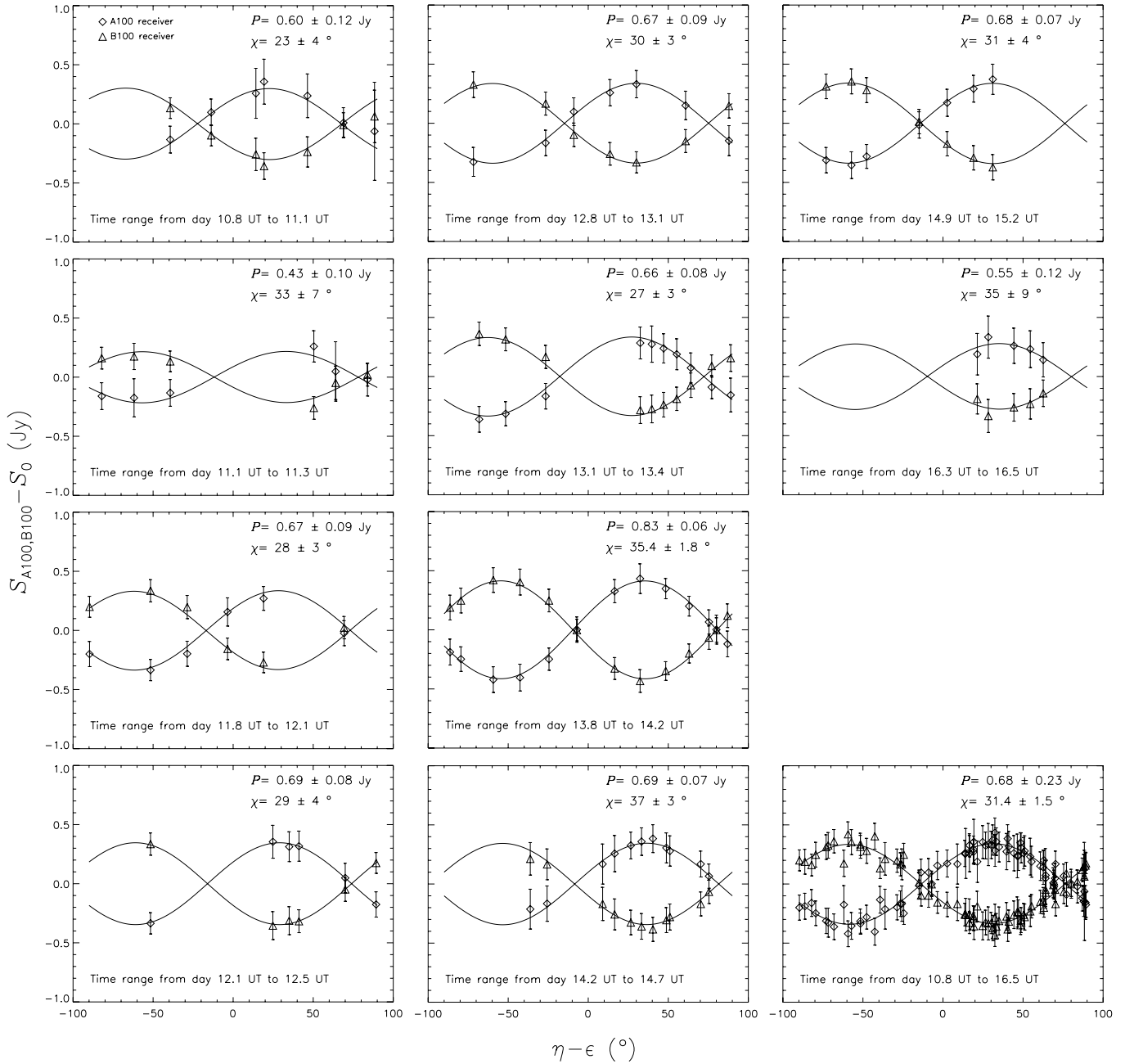


Fig. 5. Plots of the fits of functions (2) and (3) to the 86 GHz data of 0716+714. Each plot represents a time bin ≤ 12 h of observing time (labelled within each of them) with a minimum of ten data points. The time spans, ordered from top to bottom and from left to right, cover the whole observing time. The whole data set has been plotted together in the right-bottom plot. The sinusoidal lines represent the independent non-linear least squares fits of functions (2) and (3). The resulting averaged P and χ variables are given within each corresponding plot. Errors were originally computed as $1-\sigma$ uncertainties from the fits. For the right-bottom plot, the errors from the absolute total flux density and polarization angle uncertainties (see Sect. 2) have been taken into account (added in quadrature).

suggesting that the linear polarization of 0716+714 varied along our observations. The P estimates, for both 0716+714 and the secondary calibrators, are presented as a function of time in Fig. 7, while the χ evolution for 0716+714 only is shown in Fig. 8. Due to the much lower polarization degree of the calibrators, their polarization properties were optimally fitted with time bins of < 24 h. This provided one polarization measurement per day to test the stability of the secondary calibrators and it also decreased the fitting errors compared to shorter time-binnings. To allow for a better comparison with the calibrators, the 0716+714 data were also fitted using a < 24 h time binning (Fig. 7, Fig. 8 and Table 5).

While the secondary calibrators remained stable in polarization within the errors, 0716+714 displayed polarization variability during November 11 and 14. To quantify this variability, we performed a statistical analysis similar to the one presented in Sect. 3.1. Due to the much weaker polarization of the secondary calibrators compared to 0716+714, the errors of their P and especially their χ estimates are much larger than for 0716+714. Hence, in principle, it would not be reasonable to calculate m_P , m_χ , Y_P and Y_χ since they do not take into account the uncertainties on the measurements and they would not provide reliable variability results. However, the mean, the standard deviation and the reduced chi-squares of both the P and χ distributions

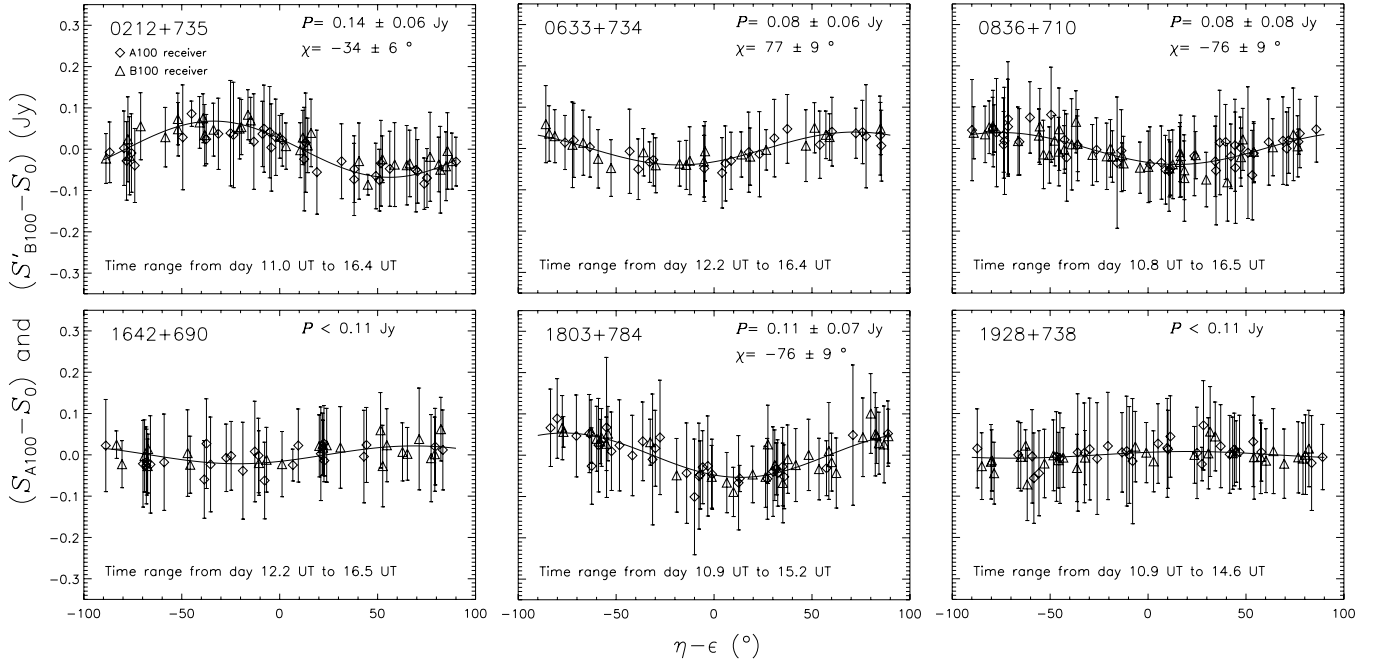


Fig. 6. 86 GHz polarization patterns of the secondary calibrators. For the sake of clarity, a shift of π rad was added to function (3) to match function (2), i.e. $S'_{B100}(i) - S_0(i) = 1/2P(i) \cos 2(\alpha(i) + \pi/2)$ (see Sect. 2.3). For each source, the data from the whole observing time-range is presented. The sinusoidal lines represent the non-linear least squares fits to the data. The resulting averaged P and χ variables are given within each corresponding plot. The errors presented on each plot were computed by adding in quadrature the $1\text{-}\sigma$ uncertainties from the fits and the errors from the absolute total flux density and polarization angle uncertainties (see Sect. 2).

Table 4. Average 86 GHz polarization properties of 0716+714 and the secondary calibrators during 2003 November 10 to 16.

Source	$\langle P \rangle$ [Jy]	$\langle p \rangle$ [%]	$\langle \chi \rangle$ [°]
0212+735	0.14 ± 0.06	12 ± 2	-34 ± 6
0633+734	0.08 ± 0.06	8 ± 3	77 ± 9
0716+714	0.68 ± 0.23	15.0 ± 1.8	31.4 ± 1.5
0836+710	0.08 ± 0.08	5.3 ± 1.6	-76 ± 9
1642+690	$0.04^{+0.07}_{-0.04}$	4 ± 4	66 ± 18
1803+784	0.11 ± 0.07	8 ± 2	-76 ± 9
1928+738	$0.02^{+0.09}_{-0.02}$	$1.1^{+1.6}_{-1.1}$...

Note: These results have been obtained, for each source, from the polarization fits over the entire time range of the observations. The errors were originally computed as $1\text{-}\sigma$ uncertainties of the polarization fits. The errors of the $\langle P \rangle$ and $\langle \chi \rangle$ measurements include those from the absolute total flux density and polarization angle uncertainties, respectively (see Sect. 2).

can still provide useful statistical information. These magnitudes are summarised in Table 5. None of the sources analysed passed the chi-squared test neither for P nor for χ . However, 0716+714 displayed relatively large values of $\chi^2_{r,P} = 2.4$ and $\chi^2_{r,\chi} = 2.2$, with corresponding variability significance levels $>95\%$. Hence, for the particular case of 0716+714 and given the relatively large significance of its polarization variability, it makes sense to compute both $m_P = 15\%$ and $m_\chi \equiv \sigma_\chi = 6^\circ$, which are attributed to the source behaviour during the first four observing days (Figs. 7 and 8).

The amount of P and χ variability of 0716+714 between each pair of adjacent measurements of these variables was characterised through their fractional variability amplitudes:

$$V_P(\Delta t_{i-1,i}) = \frac{2(P(\Delta t_i) - P(\Delta t_{i-1}))}{P(\Delta t_i) + P(\Delta t_{i-1})} \quad (5)$$

Table 5. Statistical parameters characterising the 86 GHz polarization variability of 0716+714 and the secondary calibrators, but 1928+738, during 2003 November 10–16.

Source	N	$\langle P \rangle$ [Jy]	σ_P [Jy]	$\chi^2_{r,P}$	$\langle \chi \rangle$ [°]	σ_χ [°]	$\chi^2_{r,\chi}$
0212+735	5	0.122	0.024	0.3	-33.1	6.0	0.2
0633+734	5	0.092	0.021	0.1	69.3	8.5	0.3
0716+714 ^a	10	0.648	0.103	1.8	30.9	4.3	1.7
0716+714 ^b	6	0.639	0.095	2.4	31.0	3.3	2.2
0836+710	6	0.085	0.020	0.2	-76.3	8.5	0.1
1642+690	5	0.064	0.023	0.1	54.6	17.6	0.3
1803+784	5	0.111	0.022	0.1	76.4	4.5	1.2

^a0716+714 results for ≤ 12 h.

^b0716+714 results for < 24 h are also presented to allow direct comparison with the secondary calibrators.

Note 1: $\langle P \rangle$ and $\langle \chi \rangle$ in this Table, which are based on P and χ fittings over < 24 h time bins, are less accurate than those from Table 4, which were fitted over the whole time span of the observations.

Note 2: The weak linearly polarized flux density of 1928+738 (see Table 4) does not allow us to analyse its variability.

and

$$V_\chi(\Delta t_{i-1,i}) = \frac{2(\chi(\Delta t_i) - \chi(\Delta t_{i-1}))}{\chi(\Delta t_i) + \chi(\Delta t_{i-1})}, \quad (6)$$

where Δt_i (with $i = 1, 2, \dots, 10$ for the 0716+714 polarization measurements performed with a time binning ≤ 12 h) denotes for the interval over which each one of the polarization fits was performed and $\Delta t_{i-1,i}$ symbolises the time interval between each pair of adjacent polarization measurements. We considered that an intra-day polarization variation event is significant when either V_P or V_χ is larger than its corresponding uncertainties computed by propagating the errors of P and χ . There is only one

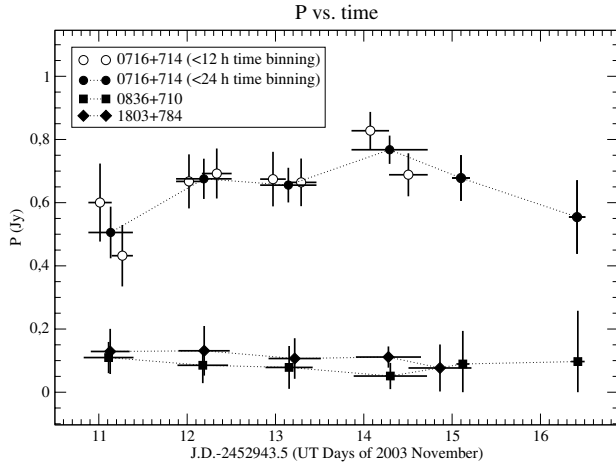


Fig. 7. 86 GHz P curves for 0716+714, 0836+710 and 1803+784. Time bins of <24 h were used for all the sources. For 0716+714 the results for time bins ≤ 12 h are also presented. Horizontal bars symbolise the time range over which each estimate of P was computed.

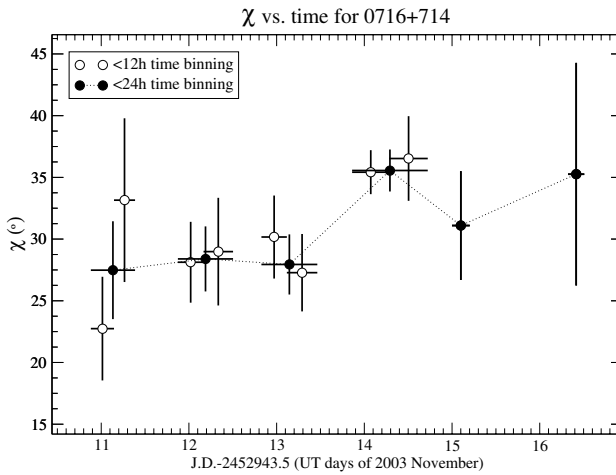


Fig. 8. 86 GHz polarization angle vs. time for 0716+714. The results obtained for time bins of both <24 h and ≤ 12 h are presented. Horizontal bars symbolise the time range over which each χ estimate was computed. For the sake of clarity, the χ time series of the calibrators (which are all constant within their corresponding errors) have not been plotted due to their large uncertainties, typically of 15° – 20° .

time interval ($\Delta t_{6,7}$) for which this condition is fulfilled. $\Delta t_{6,7}$ is a time interval of ~ 24 h on November 13–14, for which both $V_P(\Delta t_{6,7}) = (22 \pm 11)\%$ and $V_\chi(\Delta t_{6,7}) = (26 \pm 12)\%$ show a 2σ variation in P and χ , respectively (see Fig. 9). Hence, this simple analysis provided indications of IDV on the polarized emission of 0716+714 during our observations. Nevertheless, this statement should not be taken as a strong evidence of polarization IDV, as no 3σ IDV event has been detected. A future dedicated millimetre monitoring campaign, optimised for high time sampling and high polarization sensitivity, will be necessary to confirm and clarify whether 0716+714 (or any other AGN) is variable in polarization on time-scales of ≤ 24 h.

4. Discussion

4.1. Spectrum

The millimetre data presented here contributed to the assembling of the broad-band spectrum (from radio to γ -rays) of

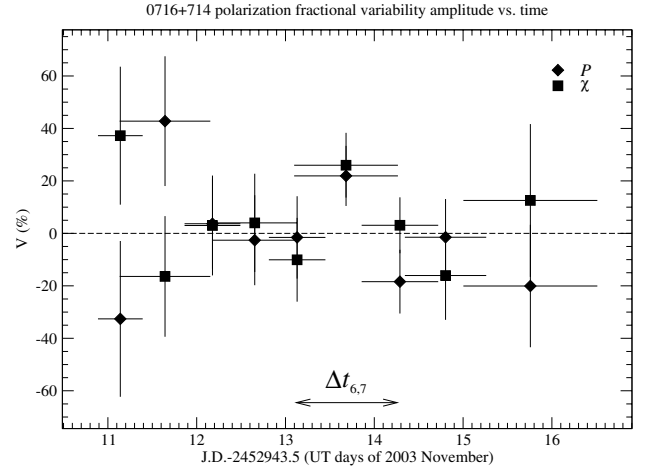


Fig. 9. Amplitude of fractional polarization variability, as a function of time. The vertical bars represent the V_P and V_χ propagated errors whereas the horizontal bars symbolise the maximum possible time range over which the variability took place. See the text for definitions.

0716+714 during November 10 to 16, 2003 presented by Ostorero et al. (2006). The spectrum was inverted between the cm- and mm-bands. Its turnover frequency (ν_m , at which the synchrotron spectrum peaks) was located at $\nu_m \approx 86$ GHz. Between 86 GHz and 667 GHz the spectrum can be fitted by a single power law with spectral index $\alpha \approx -0.3$ (where $S_\nu \propto \nu^\alpha$ and ν denotes the observing frequencies within this spectral range).

At 86 GHz, the total flux density of the source (Sect. 3.1) ranged from $S_m = 3.55 \pm 0.19$ Jy at the 10.88 UT days of November 2003 to $S_m = 5.23 \pm 0.07$ Jy at the 15.00 UT days of November 2003. The larger total flux density of the source at 86 GHz compared to that at 229 GHz, (Figs. 2 and 3) shows that the source synchrotron spectrum was optically thin between these two frequencies during the whole time range of our observations. To attempt to characterise the source spectral evolution, we have computed the spectral index for each pair of $S_{86(i)}$ and $S_{229(i)}$, where i is the index defining each one of the simultaneous 86 GHz and 229 GHz measurements. The resulting α_{86-229} evolution (shown in Fig. 10) is consistent with a decreasing pattern (spectral softening) with constant rate $\dot{\alpha}_{86-229} = (-0.03 \pm 0.02) \text{d}^{-1}$ and average $\bar{\alpha}_{86-229} = -0.23 \pm 0.10$ from the 10.88 to the 15.00 U.T. days of November 2003. However, the computed $\dot{\alpha}_{86-229}$ is not statistically significant and the possible spectral change of 0716+714 needs to be tested through more accurate spectral index data.

4.2. Intrinsic variability

Given the known frequency dependence for weak ISS, it is rather unlikely that the $Y = 34\%$ amplitude inter-day variability reported at 86 GHz is caused by this extrinsic effect. As outlined in Sect. 1, such large variability in the mm-bands can not be reproduced by the standard ISS models (e.g. Beckert et al. 2002). Fuhrmann et al. (in prep.) perform a more detailed variability study combining all the available simultaneous data from 5 GHz to 667 GHz, and show that the inter-day variations shown in this paper contradict the predictions of such models. We should hence attribute the large amplitude 86 GHz variability of 0716+714 to intrinsic causes.

Hence, the high amplitude inter-day variability reported by Ostorero et al. (2006) at 32 GHz and 37 GHz, which well matches with the millimetre behaviour shown in this paper,

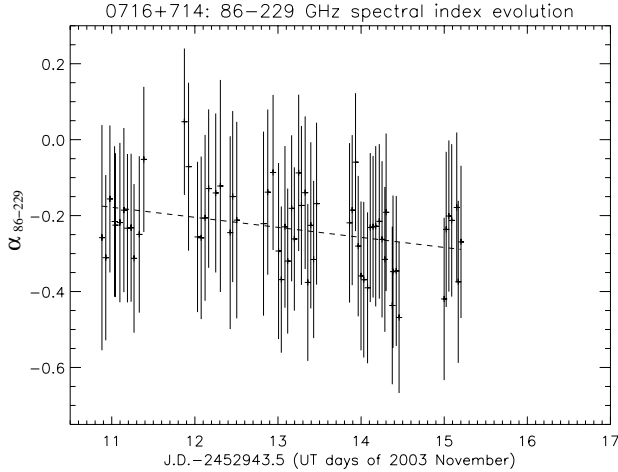


Fig. 10. Evolution of the spectral index α_{86-229} in 0716+714. The absolute total flux density calibration errors of S_{86} and S_{229} (see Sect. 2) were taken into account to compute those of α_{86-229} . The dashed line represents the best linear fit to the data, which is consistent with a pattern with a rate $\dot{\alpha}_{86-229} = (-0.03 \pm 0.02) \text{d}^{-1}$ and average $\bar{\alpha}_{86-229} = -0.23 \pm 0.10$.

was most likely produced in the source itself and not by ISS. Ostorero et al. (2006) also report on the rapid IDV in the optical range observed during the time range of our IRAM 30 m observations. Although 0716+714 did not show evidence of simultaneous radio or mm and optical IDV-time-scale transitions, as during previous monitoring campaigns (Quirrenbach et al. 1991), this can not be taken as an argument in favour of the extrinsic origin of the variability. It indicates only that, during our observations, the radio-mm emission was radiated from a different region, or through a different mechanism, than that producing the optical emission.

4.3. Brightness temperature

Under the assumption that the main component of the mm-variability is intrinsic to the source and via the causality argument, it is possible to estimate some of the physical conditions governing the source. This can be performed by modelling it as a relativistically moving homogeneous sphere (e.g. Marscher et al. 1979; Ghisellini et al. 1993). Under these assumptions, the intrinsic brightness temperature of the emitting region at the turnover frequency ν_m (at which the spectral index is zero, by definition) can be computed from its variability time scale as:

$$T_B = 1.77 \times 10^{12} \frac{S_m}{\nu_m^2 \theta_v^2} \left(\frac{1+z}{\delta} \right) \text{K}, \quad (7)$$

where S_m is the flux density of the source at the turnover frequency in Jy and ν_m is in GHz. z is the redshift of the source, δ is an equivalent Doppler factor and

$$\theta_v \lesssim 3.56 \times 10^{-4} t_v d_L^{-1} (1+z) \delta \text{ mas} \quad (8)$$

is an estimate of its angular diameter (Marscher et al. 1979) from light-travel time arguments in the absence of coherence. $t_v \equiv |\text{dln} S_\nu / \text{d}t|^{-1} = (\langle S_\nu \rangle / \Delta S_\nu) \Delta t$ is the variability time scale in days and d_L is the source luminosity distance in Gpc. In this paper, we adopt $z = 0.3$ (the lower limit for the redshift of 0716+714, see e.g. Sect. 1 and Wagner et al. 1996), a Hubble constant $H_0 = 72 \text{ km s}^{-1} \text{ Mpc}^{-1}$ and a Friedmann-Robertson-Walker cosmology with $\Omega_m = 0.3$ and $\Omega_\Lambda = 0.7$. Within these assumptions, $d_L = 1.51 \text{ Gpc}$.

Our 86 GHz observations provide us the values of $S_m = 5.23 \text{ Jy}$, $\langle S_m \rangle = 4.50 \text{ Jy}$, $\Delta S_m = 1.68 \text{ Jy}$, $\Delta t = 4.12 \text{ days}$ and $t_v = 11.1 \text{ days}$. The only remaining variable in expression (7) which can not be directly observed is δ . By assuming a non-moving source, expression (7) gives us the apparent brightness temperature $T_B^{\text{app}} \equiv T_B(\delta = 1) > 1.4 \times 10^{14} \text{ K}$ at $z = 0.3$, which exceeds by more than two orders of magnitude the IC-limit $T_{B,IC}^{\text{lim}} \approx 10^{12} \text{ K}$ (Kellermann & Pauliny-Toth 1969). Hence, $T_{B,IC}^{\text{lim}}$ sets a lower limit to the Doppler factor of the emitting region, which should then be $\delta_{T_B} > 5.2$. Note that a more accurate limit for $T_{B,IC}^{\text{lim}}$ (of $\sim 3 \times 10^{11} \text{ K}$) was computed by Readhead (1994) (see also Kellermann 2003). To avoid the violation of the latter, $\delta_{T_B} > 7.8$ is required.

4.4. Angular size

The latter constraint ($\delta_{T_B} > 7.8$), together with expression (8), allows us to estimate an upper limit for the size of the emitting region responsible for the variability during our observations, which should be $\theta_{T_B} < 0.03 \text{ mas}$. Obviously, θ_{T_B} is also an upper limit for the maximum size of such region obtained from $\delta_{T_B} > 5.2$.

It should be stressed that θ_{T_B} does not account for the size of the whole source, but only for the region responsible for the rapid variability, which in the case of 0716+714 has been associated with the VLBI core component of its relativistic jet (Bach et al. 2006).

An independent constraint on the size of the variability region can be obtained from the 86 GHz VLBI observations of 0716+714 performed by Bach et al. (2006) in April 2003. A Gaussian model fit of their resulting image gives a FWHM size of the 86 GHz VLBI core of 0.014 mas, which is much lower than the minimum beam size of VLBI observations at such frequency ($\sim 0.04 \text{ mas}$; e.g. Agudo et al. 2005). This gives us $\theta_{\text{VLBI}} < 0.04 \text{ mas}$, which is in agreement with our estimate of θ_{T_B} .

We will hence assume hereafter that the true angular size of the rapid variability region is $\theta_v = \theta_{T_B} < 0.03 \text{ mas}$.

4.5. Inverse Compton Doppler factor

It is also possible to compare the expected and the observed first order self-Compton γ -ray flux density to constrain the IC Doppler factor (δ_{IC}) of the source (Marscher 1983 and Ghisellini et al. 1993). δ_{IC} is defined as:

$$\delta_{IC} = f(\alpha) S_m \left[\frac{\ln(\nu_2/\nu_m) \nu_\gamma^\alpha}{S_\gamma \theta_v^{(6-4\alpha)} \nu_m^{(5-3\alpha)}} \right]^{1/(4-2\alpha)} (1+z), \quad (9)$$

where α is the spectral index of the optically thin synchrotron spectrum ($\alpha = -0.3$ has been adopted here), $f(\alpha) = 0.14 - 0.08\alpha$ (Ghisellini et al. 1993 and references therein), ν_2 is the upper frequency cut-off of the synchrotron spectrum in GHz, ν_γ is the γ -ray energy in keV and S_γ is the measured γ -ray flux at ν_γ in Jy. ν_2 , in GHz, is the most poorly known variable among those in Eq. (9). However, this problem is overcome by the fact that δ_{IC} is a weak function of ν_2 , which is contained within a logarithmic factor. Here, we have assumed $\nu_2 = 10^6 \text{ GHz}$ (Biermann & Strittmatter 1987). Implicit to Eq. (9) is the assumption that the electrons radiating the synchrotron emission have a power-law energy distribution ($N(E) = N_0 E^{2\alpha-1}$, with $h\nu_m \lesssim E \lesssim h\nu_2$) and that the magnetic field is tangled in the rest frame of the emitting plasma.

Table 6. Physical parameter estimates. See the text for definitions.

Parameter	Value	Assumptions
For $z = 0.3$, $d_L = 1510$ Mpc, $S_m = 5.23$ Jy, $t_v = 11.1$ days		
T_B^{app}	$>1.4 \times 10^{14}$ K	$\delta = 1$
δ_{T_B}	>5.2	$T_{B,IC}^{\text{lim}} = 10^{12}$ K
δ_{T_B}	>7.8	$T_{B,IC}^{\text{lim}} = 3 \times 10^{11}$ K
θ_{T_B}	<0.03 mas	$\delta > 7.8$
θ_{VLBI}	<0.04 mas	86 GHz VLBI beam-size
θ_v	<0.03 mas	
$\delta_{IC,8\text{keV}}$	>15.8	$S_{8\text{keV}} < 1.37 \times 10^{-7}$ Jy, $\alpha = -0.3$
$\delta_{IC,23\text{keV}}$	>14.6	$S_{23\text{keV}} < 2.55 \times 10^{-7}$ Jy, $\alpha = -0.3$
$\delta_{IC,63\text{keV}}$	>15.1	$S_{63\text{keV}} < 1.23 \times 10^{-7}$ Jy, $\alpha = -0.3$
$\delta_{IC,141\text{keV}}$	>14.0	$S_{141\text{keV}} < 2.42 \times 10^{-7}$ Jy, $\alpha = -0.3$

By taking into account the dependence of θ_v on δ in (9), δ_{IC} can be written as:

$$\delta_{IC} \gtrsim \left\{ \frac{\ln(\nu_2/\nu_m) \nu_\gamma^\alpha [f(\alpha) S_m (1+z)]^{(4-2\alpha)}}{S_\gamma \Theta_v^{(6-4\alpha)} \nu_m^{(5-3\alpha)}} \right\}^{1/(10-6\alpha)}, \quad (10)$$

where we have defined $\Theta_v \equiv 3.56 \times 10^{-4} t_v d_L^{-1} (1+z)$ mas.

The results of the simultaneous INTEGRAL soft γ -ray observations of 0716+714 reported by Ostorero et al. (2006) ($F_{3-35\text{keV}} < 6.12 \times 10^{-12}$ erg cm $^{-2}$ s $^{-1}$, $F_{15-40\text{keV}} < 1.41 \times 10^{-11}$ erg cm $^{-2}$ s $^{-1}$, $F_{40-100\text{keV}} < 1.72 \times 10^{-11}$ erg cm $^{-2}$ s $^{-1}$ and $F_{100-200\text{keV}} < 5.73 \times 10^{-11}$ erg cm $^{-2}$ s $^{-1}$; see also Table 6 for the corresponding flux densities in Jy), together with expression (10), allow us to set new constraints on the Doppler factor of 0716+714 during our observations. Assuming $t_v = 11.1$ days as in Sect. 4.3, we derive lower limits of $\delta_{IC,8\text{keV}} > 15.8$, $\delta_{IC,23\text{keV}} > 14.6$, $\delta_{IC,63\text{keV}} > 15.1$ and $\delta_{IC,141\text{keV}} > 14.0$ from the upper limits of the flux densities of the source at 8 keV, 23 keV, 63 keV and 141 keV, respectively.

It is worth to note that, for $\alpha = -0.3$, expression (10) is a weak function of the redshift and the luminosity distance of the source ($\delta_{IC} \propto (1+z)^{-0.2} d_L^{0.6}$). Hence, the constraint on the Doppler factor of the source provided by (10), $\delta_{IC} > 14.0$, is more robust than those derived from expression (7) and the limits for T_B (Sect. 4.3).

5. Conclusions

We have presented the results from millimetre observations of 0716+714, which were performed on 2003 November 10 to 18 with the IRAM 30 m telescope. Our observation strategy, based on the rapid time sampling of both the target source and the calibrators, enabled us to reach a relative calibration accuracy of 1.2% at 86 GHz, which demonstrates the good performance of this telescope and its ability for future accurate IDV studies in the millimetre range.

During our first four observing days, the source displayed large amplitude ($Y = 34\%$) and monotonous inter-day variability at 86 GHz. As such large amplitude variability is not expected to be produced by standard ISS at mm wavelengths (Rickett et al. 1995), this variation should be considered as intrinsic to the source and not due to the influence of the interstellar medium. The similar 32 GHz and 37 GHz behaviour reported by Ostorero et al. (2006) during the same observing time range could hence be explained by intrinsic causes also.

Ostorero et al. (2006) also report clear evidence of IDV in the optical range, which is not matched either in the mm or in the cm

bands (see also Fuhrmann et al. in prep.). This indicates that the radio-mm emitting region was located in a different region than the optical one or that their radiation behaviours were driven by different physical processes during our observations.

We have reported an unusually large linear polarization degree $\langle p \rangle = (15.0 \pm 1.8)\%$ of 0716+714 at 86 GHz, which suggests a large level of magnetic field alignment. At such frequency, linear polarization inter-day variability, with significance level $\gtrsim 95\%$; $\sigma_P/\langle P \rangle = 15\%$ and $\sigma_\chi = 6^\circ$, was observed during the first four observing days. We have also shown 2σ evidence of simultaneous polarization flux density and polarization angle IDV within a time $\lesssim 24$ h. If such rapid polarization variations that are uncorrelated with the total flux density variability are confirmed by future observations, then equally rapid changes of the magnetic field configuration of the source or changes of opacity around ν_m would be required to explain the phenomenon. In both cases, inhomogeneous models would probably have to be invoked.

The synchrotron spectrum of 0716+714 peaked at $\nu_m \approx 86$ GHz during 2003 November 10 to 15 (Ostorero et al. 2006), and showed an optically thin spectral index $\bar{\alpha}_{86-229} = -0.23 \pm 0.10$ between 86 GHz and 229 GHz. The apparent brightness temperature derived from our 86 GHz light curve, $T_B^{\text{app}} > 1.4 \times 10^{14}$ K for a redshift $z = 0.3$, exceeds, at least by two orders of magnitude, the IC-limit of 3×10^{11} K (Kellermann & Pauliny-Toth 1969; Readhead 1994; Kellermann 2003). This mismatch can be explained by the relativistic motion or expansion of the source with a minimum Doppler factor $\delta > 7.8$. The upper limits from the soft γ -ray simultaneous INTEGRAL observations in the 3 keV to 200 keV energy range enabled us to compute an independent and more robust limit for the source Doppler factor, $\delta_{IC} \gtrsim 14$. This limit is consistent with previous estimates of the Doppler factor of 0716+714 measured from the kinematics of VLBI-scale jet features (Bach et al. 2005), which ranged from $\delta_{VLBI} = 20$ to $\delta_{VLBI} = 30$. Such high Doppler factors have also been measured with 43 GHz-VLBI by Jorstad et al. (2005), who detected $\delta_{VLBI} > 20$ in 9 of the 13 monitored blazars.

As no soft- γ -ray IC-avalanches were detected by INTEGRAL during our observations and the reported large amplitude 86 GHz variability can not be ascribed to the ISS, the relativistic beaming of the radiation coming from the emitting region in 0716+714 offers a robust explanation of the apparent violation of the IC-limit of the brightness temperature in the mm range. Note, however, that (total or partial) coherent synchrotron-emission scenarios can not be ruled out.

Finally, we should stress that we have proven that 0716+714, in particular, and blazars, in general, can display apparent brightness temperatures two orders of magnitude larger than the theoretical limits in the millimetre range and that the influence of the interstellar medium is not always necessary to explain the mismatch between observations and theory. Following the above arguments, we are rather confident that, apart from inaccuracies in our assumptions, the estimates and limits for the physical parameters of 0716+714 reported in the previous sections correspond to those governing the observed source behaviour.

Acknowledgements. We gratefully acknowledge A. L. Roy, A. P. Marscher and A. P. Lobanov for their helpful suggestions on this paper, C. Thum and H. Wiesemeyer for their useful comments and information on polarization calibration of IRAM 30 m telescope data and A. Sievers for his help in the calibration of our data. We also wish to acknowledge helpful comments by the anonymous referee. I. Agudo, E. Angelakis, L. Fuhrmann, U. Bach, L. Ostorero and J. Gracia acknowledge financial support from the EU Commission under contract HPRN-CT-2002-00321 (ENIGMA network). This paper is based on

observations carried out at the IRAM 30 m telescope. IRAM is supported by INSU/CNRS (France), MPG (Germany) and IGN (Spain).

References

- Agudo, I., Krichbaum, T., Bach, U., et al. 2005, RMxAA, in press [arXiv:astro-ph/0511268]
- Aller, M. F., Aller, H. D., Hughes, P. A., & Latimer, G. E. 1999, ApJ, 512, 601
- Bach, U., Krichbaum, T. P., Ros, E., et al. 2005, A&A, 433, 815
- Bach, U., Krichbaum, T. P., Kraus, A., et al. 2006, A&A, 452, 83
- Beckert, T., Fuhrmann, L., Cimò, G., et al. 2002, in Proceedings of the 6th EVN Symposium, ed. E. Ros, R. W. Porcas, A. P. Lobanov, & J. A. Zensus, 79
- Benford, G. 1992, ApJ, 391, L59
- Biermann, P. L., & Strittmatter, P. A. 1987, ApJ, 332, 643
- Fuhrmann, L., et al., A&A, in prep.
- Ghisellini, G., Padovani, P., Celotti, A., & Maraschi, L. 1993, ApJ, 407, 65
- Greve, A., Neri, R., & Sievers, A. 1998, A&AS, 132, 413
- Gómez, J. L., Alberdi, A., & Marcaide, J. M. 1993, A&A, 274, 55
- Griffin, M. J., & Orton, G. S. 1993, Icar, 105, 537
- Heeschen, D. S., Krichbaum, T. P., Schalinski, C. J., & Witzel, A. 1987, AJ, 94, 1493
- Homan, D. C., & Lister, M. L. 2006, AJ, 131, 1262
- Jorstad, S. G., Marscher, A. P., Lister, M. L., et al. 2005, AJ, 130, 1418
- Kedziora-Chudczer, L. L., Jauncey, D. L., Wieringa, M. H., Tzioumis, A. K., & Reynolds, J. E. 2001, MNRAS, 325, 1411
- Kellermann, K. I., & Pauliny-Toth, I. I. K. 1969, ApJ, 155, L71
- Kellermann, K. I. 2003, in Radio Astronomy at the Fringe, ed. J. A. Zensus, M. H. Cohen, & E. Ros, ASP Conf. Ser., 300, 185
- Kramer, C. 1997, IRAM report (Calibration procedures and efficiencies, www.iram.es/IRAMES/otherDocuments/manuals/Index.html)
- Kraus, A., Krichbaum, T. P., & Witzel, A. 1999a, in BL Lac phenomenon, ed. L. Takalo, & A. Sillanpää, ASP Conf. Ser., 159, 49
- Kraus, A., Witzel, A., & Krichbaum, T. P. 1999b, New Astron. Rev., 43, 685
- Kraus, A., Krichbaum, T. P., Wegner, R., et al. 2003, 401, 161
- Kraus, J. D. 1986, Radio Astronomy (Cygnus-Quasar Books, Powell)
- Kutner, M. L., & Ulich, B. L. 1981, ApJ, 250, 341
- Lisenfeld, U., Thum, C., Neri, R., & Sievers, A. 2000, IRAM report (Secondary calibrators for continuum measurements in the 1.3 mm window at the IRAM 30 m telescope, www.iram.es/IRAMES/otherDocuments/manuals/Index.html)
- Lovell, J. E. J., Jauncey, D. L., Bignall, H. E., et al. 2003, AJ, 26, 1699
- Macquart, J. P., Kedziora-Chudczer, L., Rayner, D. P., & Jauncey, D. L. 2000, ApJ, 538, 623
- Marscher, A. P. 1983, ApJ, 264, 296
- Marscher, A. P., Marshall, F. E., Mushotzky, R. F., et al. 1979, ApJ, 233, 498
- Ostorero, L., Wagner, S. J., Gracia, J., et al. 2006, A&A, in press [arXiv:astro-ph/0602237]
- Otterbein, K., & Wagner, S. 1999, in BL Lac phenomenon, ed. L. Takalo, & A. Sillanpää, ASP Conf. Ser., 159, 289
- Pacholczyk, A. G. 1970, Radio Astrophysics: Nonthermal Processes in Galactic and Extragalactic Sources (San Francisco: W. H. Freeman and Company)
- Qian, S.-J., Li, X.-C., Wegner, R., Witzel, A., & Krichbaum, T. P. 1996, ChA&A, 20, 15
- Qian, S.-J., Kraus, A., Zhang, X.-Z., et al. 2002, ChJAA, 2, 325
- Quirrenbach, A., Witzel, A., Qian, S. J., et al. 1989, A&A, 226, L1
- Quirrenbach, A., Witzel, A., Wagner, S., et al. 1991, ApJ, 372, L71
- Quirrenbach, A., Witzel, A., Krichbaum, T. P., et al. 1992, A&A, 258, 279
- Quirrenbach, A., Kraus, A., Witzel, A., et al. 2000, A&AS, 141, 221
- Raiteri, C. M., Villata, M., Tosti, G., et al. 2003, A&A, 402, 151
- Readhead, A. C. S. 1994, ApJ, 426, 51
- Rees, M. 1966, MNRAS, 135, 345
- Rickett, B. J. 1990, ARA&A, 28, 561
- Rickett, B. J., Quirrenbach, A., Wegner, R., Krichbaum, T. P., & Witzel, A. 1995, A&A, 293, 479
- Thum, C., Morris, D., Navarro, S., & Sievers, A. 2000, IRAM report (www.iram.fr/~thum/ifpol_04.ps.gz)
- Thum, C., Wiesemeyer, H., Morris, D., Navarro, S., & Torres, M. 2003, in Proceedings of the SPIE, Polarimetry in Astronomy, ed. S. Fineschi, 4843, 272 (www.iram.fr/~thum/spie.ps.gz)
- Wagner, S. J., Sanchez-Pons, F., Quirrenbach, A., & Witzel, A. 1990, A&A, 235, 1
- Wagner, S. J., & Witzel, A. 1995, ARA&A, 33, 163
- Wagner, S. J., Witzel, A., Heidt, J., et al. 1996, AJ, 111, 2187
- Wild, W. 1999, IRAM report (The 30 m manual) (www.iram.es/IRAMES/otherDocuments/manuals/Index.html)
- Witzel, A., Heeschen, D. S., Schalinski, C. J., & Krichbaum, T. P. 1986, Mitt. Astron. Ges., 65, 239

Online Material

Appendix A: Response of the IRAM 30 m heterodyne receivers to a partially linearly polarized wave

The power received by an antenna when it observes a source of arbitrary polarization can be characterised as

$$W = \frac{1}{2}S_0A_e(1-d) + S_0A_ed\cos^2\frac{\gamma}{2}, \quad (\text{A.1})$$

where S_0 is the total flux density of the source, A_e is the effective aperture of the antenna, d the source degree of polarization and γ the angle between the wave and the antenna polarization states on the Poincaré sphere (see e.g. Kraus 1986). The first and second terms on the right-hand side of Eq. (A.1) represent the unpolarized and polarized responses of the antenna, respectively.

If the polarized component of the incident radiation is only linearly polarized, then d is the degree of linear polarization (p). In addition, for the case of the IRAM 30 m millimetre radio telescope, when heterodyne receivers are used, $\gamma \equiv \alpha + \beta$. Here, α is the angle between the polarization direction of the incident signal and the horizontal direction in the telescope receiver cabin -the x axis of the reference polarization plane, see Fig. A.1-. β is the angle between the x axis and the polarization orientation of the receiver. For the particular case of receivers A100 and B100, β is $\pi/2$ and 0, respectively.

Taking into account that $W = kT_A^*$ and $T_A^*/S_{\text{obs}} = A_e/(2k)$, where k is the Boltzmann constant, T_A^* is the calibrated antenna temperature outlined on Sect. 2.2 and S_{obs} is an equivalent total flux density observed for the receiver, Eq. (A.1) may be expressed for A100 and B100 as:

$$S_{A100}(t) = S_0(t)(1-p(t)) + 2S_0(t)p(t)\sin^2(\alpha(t)) \quad (\text{A.2})$$

and

$$S_{B100}(t) = S_0(t)(1-p(t)) + 2S_0(t)p(t)\cos^2(\alpha(t)). \quad (\text{A.3})$$

where we have introduced the possible time dependence of each variable and we have defined $S_{A100}(t) \equiv S_{\text{obs}}(\alpha(t), \beta = \pi/2, t)$ and $S_{B100}(t) \equiv S_{\text{obs}}(\alpha(t), \beta = 0, t)$. From (A.2) and (A.3) and defining the linearly polarized flux density of the observed source as $P \equiv S_0p$, then it is straightforward to show that:

$$\frac{S_{A100}(t) + S_{B100}(t)}{2} = S_0(t), \quad (\text{A.4})$$

$$S_{A100}(t) - S_0(t) = P(t)\cos 2\left(\alpha(t) + \frac{\pi}{2}\right) \quad (\text{A.5})$$

and

$$S_{B100}(t) - S_0(t) = P(t)\cos 2(\alpha(t)), \quad (\text{A.6})$$

Thum et al. (2000) showed that, for the IRAM 30 m telescope, $\alpha(t)$ can be expressed as the following function of astronomical angles:

$$\alpha(t) = \frac{\pi}{2} - \chi(t) + \eta(t) - \epsilon(t), \quad (\text{A.7})$$

(see also Fig. A.1) where $\chi(t)$ is the electric vector position angle of the source (defined from north to east in the equatorial coordinate system (RA, Dec)) and $\eta(t)$ and $\epsilon(t)$ are, respectively, the parallactic angle and elevation angles (see Fig. A.1 and, Thum et al. 2000). Note that the location of the receiver cabin in the Nasmyth focus of the IRAM 30 m telescope causes a rotation of the equatorial reference system by an angle $\chi_0(t) = \epsilon(t) - \eta(t)$ with regard to the polarization reference system (x, y).

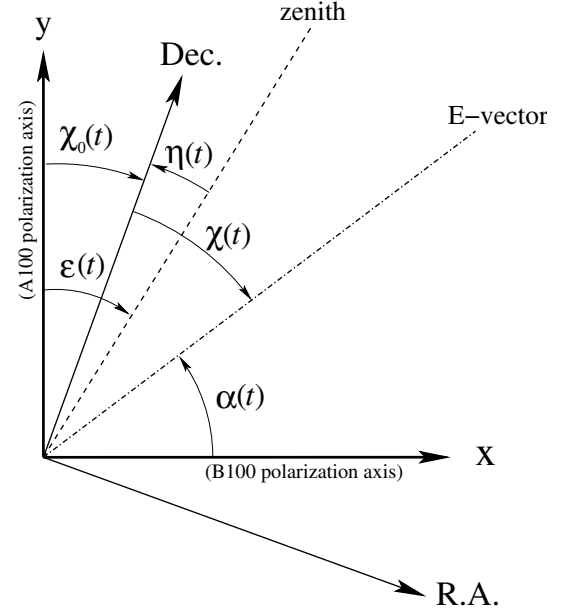


Fig. A.1. Angles in the reference polarization plane (x, y) as seen from the A100 and B100, IRAM 30 m heterodyne receivers. $\alpha(t)$, which is defined in (x, y) and can be measured by fitting Eqs. (A.5) and (A.6), relates to the astronomical electric vector position angle $\chi(t)$ (defined from north to east in the equatorial coordinate system (RA, Dec), to the parallactic angle $\eta(t)$ and to the elevation angle $\epsilon(t)$.

Appendix B: Statistical formulation for variability

The statistical variables used in this paper are defined in detail by Quirrenbach et al. (2000) and Kraus et al. (2003). Here we present a summary of these definitions.

The modulation index,

$$m[\%] = 100\frac{\sigma_S}{\langle S \rangle}, \quad (\text{B.1})$$

(where σ_S is the standard deviation of the flux density measurements and $\langle S \rangle$ is its average in time) provides the strength of the observed variability amplitude of each source without taking into account the uncertainty of the measurements.

The variability amplitude,

$$Y[\%] = 3\sqrt{m^2 - m_0^2}, \quad (\text{B.2})$$

(where m_0 is the modulation index of the non-variable and nearby calibrators) gives a measurement of the variability amplitude with regard to that of the non-variable calibrators, for which Y is set to zero.

The reduced chi-squared,

$$\chi_r^2 = \frac{1}{N-1} \sum_{i=1}^N \left(\frac{S_i - \langle S \rangle}{\Delta S_i} \right)^2, \quad (\text{B.3})$$

(where N is the number of measurements, the S_i are the individual flux densities and Δ_i their errors) tests the hypothesis that the measured light curves could be modelled by a constant function. We consider that a source is variable (with a significance level $\geq 99.9\%$) only if its light curve shows a probability to be constant $\leq 0.1\%$.

Finally, the structure function is defined as

$$D(\tau) = \langle (S(t) - S(t+\tau))^2 \rangle, \quad (\text{B.4})$$

(with $\langle \rangle$ denoting averaging in time). A characteristic time-scale in the light curves (i.e., the time between a maximum and a minimum or vice-versa) causes a maximum in $D(\tau)$, while a periodic pattern produces a minimum.